

Nanoscale

Accepted Manuscript



This is an *Accepted Manuscript*, which has been through the Royal Society of Chemistry peer review process and has been accepted for publication.

Accepted Manuscripts are published online shortly after acceptance, before technical editing, formatting and proof reading. Using this free service, authors can make their results available to the community, in citable form, before we publish the edited article. We will replace this *Accepted Manuscript* with the edited and formatted *Advance Article* as soon as it is available.

You can find more information about *Accepted Manuscripts* in the [Information for Authors](#).

Please note that technical editing may introduce minor changes to the text and/or graphics, which may alter content. The journal's standard [Terms & Conditions](#) and the [Ethical guidelines](#) still apply. In no event shall the Royal Society of Chemistry be held responsible for any errors or omissions in this *Accepted Manuscript* or any consequences arising from the use of any information it contains.

ARTICLE

Carbon Nanotube-Bonded Graphene Hybrid Aerogels and an Application to Water Purification

Cite this: DOI: 10.1039/x0xx00000x

Byeongho Lee^a, Sangil Lee^a, Minwoo Lee^b, Dae Hong Jeong^b, Youngbin Baek^c, Jeyong Yoon^c, and Yong Hyup Kim^{a*}Received 00th January 2012,
Accepted 00th January 2012

DOI: 10.1039/x0xx00000x

www.rsc.org/

We present carbon nanotube (CNT)-bonded graphene hybrid aerogels that are prepared by growing CNTs on graphene aerogel surface with nickel catalyst. With the presence of bonded CNTs in graphene aerogel, vastly improved mechanical and electrical properties result. A significant increase in specific surface area is also realized. The presence of CNTs transforms the hybrid aerogels into a mesoporous material. Viscoelasticity of the hybrid aerogels are found to be invariant with respect to temperature over a range between -150 °C and 450 °C. These characteristics along with improved properties would make the hybrid aerogels an entirely different class of material for applications in the fields of biotechnology and electrochemistry. Mesoporous nature of the material along with a high specific surface area also makes the hybrid aerogel attractive as a water treatment substance. Both anionic and cationic dyes can be removed effectively from water with the hybrid aerogel. A number of organics and oils can selectively be separated from water by the hybrid aerogel. The hybrid aerogel is easy to handle and separate due to its magnetic nature, and can readily be recycled and reused.

Introduction

Graphene hydrogel was initially introduced as a biocompatible carbon material that is attractive in the fields of biotechnology and electrochemistry, such as drug-delivery, tissue scaffolds, bionic nanocomposites, and supercapacitors.¹ It can simply be turned into graphene aerogel by freeze-drying. Since then, graphene aerogel has found applications as electrode for supercapacitor² and lithium ion battery,³ electrocatalyst for ethanol fuel cell,⁴ sensor material,⁵ and efficient absorbent of oil.⁶

For the graphene aerogel to reach its rightful potential, however, its relatively poor electrical and mechanical properties need to be improved. Theoretical and experimental studies have indicated that three dimensional (3D) pillared nano-carbon architectures, consisting of parallel graphene layers supported by vertically aligned carbon nanotubes in between, possess desirable out-of-plane electron transport and mechanical properties that are not present in the architectures consisting only of graphene sheets. The unique synergistic effect of one-dimensional CNTs and two-dimensional graphene sheets has indeed been observed for nano-carbon hybrid materials in the form of sheets.⁷⁻¹⁴ In many applications, however, aerogels are preferable to sheets as they are highly porous, readily compressible and squeezable,^{15, 16} and three-dimensionally

mesoporous. Therefore, CNT-bonded graphene hybrid aerogels, which may integrate the intrinsic properties of graphene and CNT, together with unique characteristics of aerogel, could provide an intriguing 3D macroscopic architecture with attractive structures and properties. Despite the advantages, there has not been any attempt to produce hybrid aerogel of CNT-bonded graphene although there have been numerous efforts to produce CNT-graphene hybrid, bonded and non-bonded¹⁷⁻²²

In this work, we introduce CNT-bonded graphene hybrid aerogels. We find the hybrid aerogels to deliver vastly improved mechanical and electrical properties and large surface area as originally envisioned. They also present intriguing properties that were unforeseen at the outset. Improved mechanical property and large surface area are essential features of a good membrane for water purification, the former for maintaining mechanical integrity of the membrane under suction for the purification and the latter for enhancing the impurity removal capacity. For these reasons, we demonstrate the utility of the hybrid aerogels as adsorbents for removing harmful dyes. We find the hybrid material to be amphoteric, removing not only anionic dyes but also cationic ones.

Experimental

Preparation of CNT-bonded graphene hybrid aerogel. GO was prepared from graphite powders according to Hummers' method.²³ In a typical synthesis, a certain amount of NiCl₂·6H₂O powder (sigma aldrich) was quickly added into DI water (concentration: 1.2 mmol) and then sonicated for about 30 min. 2.5 ml of the NiCl₂ aqueous solution was added into 2.5 ml of a 4 mg ml⁻¹ GO aqueous suspension stored in a transparent cylindrical vial. The resulting mixture is sonicated for 30 min to form a homogeneous NiCl₂/GO mixture. The vial containing the mixture solution is clamped between teflon plates and then placed in vacuum oven for 6 hours at 150 °C to form 3D graphene hydrogels. The hydrogel was taken out and freeze-dried into 3D graphene-Metal Salts (NiCl₂) hybrid structure (G-MS).

The growth of CNTs was conducted on the NiCl₂ loaded G-MS hybrid structure as precursor using water-assisted thermal CVD method. The G-CNT_A hybrid structure was synthesized by G-MS treated in quartz tube at 810 °C (at ramp rate of 810 °C/min) for 60 min with C₂H₂ (330 sccm) as a carbon source, Ar (480 sccm) as a carrier gas, H₂ (90 sccm) as a reduction agent of metal salts and H₂O vapor generated by bubbling water at 60 °C with Ar flow (140 sccm) as growth enhancer. Also, G-MS for synthesizing the G-MN hybrid structure was heated at 810 °C for 15 min (at ramp rate of 40.5 °C/min) for forming the metallic nano-particles with homogeneous size with Ar (480 sccm) as a carrier gas and H₂ (90 sccm) as a reduction agent of metal salts. The G-CNT_B hybrid structure was synthesized by treating the G-MN hybrid structure at the same CVD condition as the G-CNT_A.

Dye adsorption experiments. Two basic dyes (methylene blue and crystal violet), one direct dye (congo red) and acid dye (methyl orange) are employed to investigate the adsorption behavior of the G-CNT_A. In typical experiment, the G-CNT_A (10 mg) is added in to aqueous dye solution (30 mg/L) followed by slowly stirring at room temperature. Before mixing, a few droplets of ethanol is dropped onto the surface of the 3D graphene hybrid structures in order to facilitate absorption of the aqueous dye solutions into the structures.²⁴ At a series of intervals, the mixture is sampled and the dye concentration remaining in the mixture was measured after concentration. The dye concentration is determined through a UV-Vis spectrometer at the maximum absorbance of each dye (MO: 464, CR: 498, CV: 586, MB: 670 nm). The amount of dye q_t (mg/g) absorbed with the aerogel at time t , was calculated using the following equation.

$$q_t = \frac{(c_0 - c_t)V}{m} \quad (1)$$

Where c_0 and c_t (mg/L) are the concentration of dye initially and at time t , V is the volume of dye solution (L), and m is the mass of adsorbent used (g).

Cetyl trimethylammonium bromide (CTAB) is chosen as the regenerant to investigate the desorption behavior of the loaded dye within the G-CNT_A. After adsorption, the adsorbent containing the adsorbed dye is added into 200 mL of DI water and 200 mg of CTAB is added into above suspension to desorb the dye from the structure.

Characterization. The microstructures of the hybrid structures based on graphene sheets are characterized by scanning electron microscope (SEM) images, taken with a Hitach S-48000 FE-SEM at an acceleration voltage of 15 kV, and transmission electron microscope (TEM) images by a JEOL JEM-3000F transmission electron microscope at an

acceleration voltage of 300 kV. For revealing the compositions of the hybrid structures, X-ray diffraction (XRD) analysis was performed on a Bruker New D8-advance X-ray diffractometer equipped with Ge-monochromatized Cu K α radiation ($\lambda = 1.5418 \text{ \AA}$). The Raman spectra were conducted on a confocal laser micro Raman spectrometer with a 532 nm laser source. (LabRam 300, JY-Horiba) and 100X objective lens. EDS spectra and elemental composition in Table S1 were measured by Carl Zeiss SUPRA 55VP FE-SEM. The inset images in Figure S7 were measured with Tecnai F20 analytical TEM at an acceleration voltage of 200 kV. The specific surface area (S_{BET}) was determined according to the Brunauer-Emmett-Teller (BET) method at 77 K using micromeritics ASAP 2010. The magnetic properties of the hybrid structures were investigated using a Vibrating Sample Magnetometer (VSM, Lake shore cryotronics, USA) at room temperature. Also, Young's modulus of the hybrid structures is determined from compressive stress-strain curve acquired by measuring the force applied to the structures under compressive strain with Japan Instrumentation system's automatic stand equipped with handy-type force gauge. The I-V measurements were performed at room temperature using two-point probe station (MS Tech, South Korea) and the electrical conductivity of the structures can be calculated from the data of the I-V curve by considering the structure size. The viscoelastic properties were examined using Mattler-Toledo Dynamic Mechanical Thermal Analyzer with compression clamp. The tests were carried out to 9% compressive strain at compressive stress 1 kPa and frequency 1 Hz in case of room temperature tests and at temperature from -150 °C to 450 °C in a chamber at compressive strain 3%, compressive stress 1 kPa, frequency 1 Hz in case of the temperature variation tests. The UV-vis spectra of dye solutions before and after adsorption tests were acquired with optizen pop QX instrument (South Korea).

Results and discussion

Graphene aerogel is typically prepared by hydrothermal treatment of graphene oxide nanoparticles, followed by freeze-drying of the graphene hydrogel thus formed.¹ To form a 3D

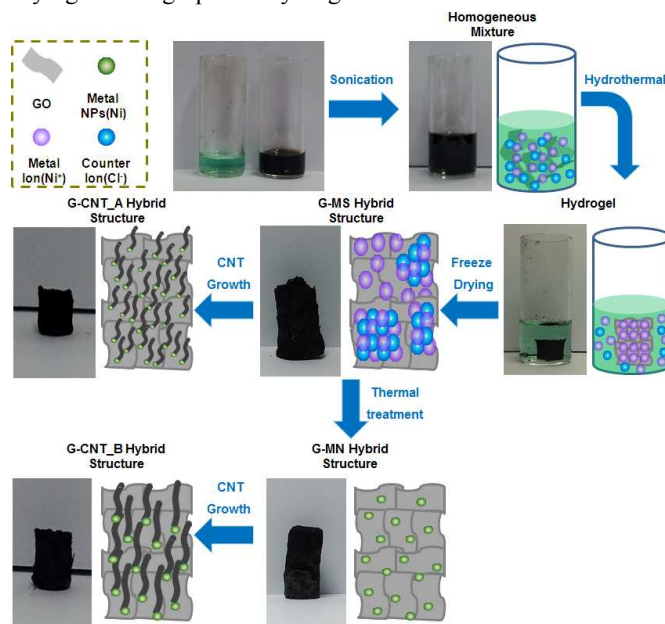


Figure 1. Schematic illustration of process for fabricating the 3D graphene-CNTs hybrid structures.

CNT-bonded graphene aerogel, carbon nanotubes have to be grown on the graphene aerogel, which requires a catalyst for the CNT growth. A catalyst precursor could be incorporated into the aerogel by impregnation. However, the manner in which the catalyst is prepared and loaded onto the surface would have an impact on the characteristics of the CNT-bonded graphene aerogel. Inclusion of the precursor in the graphene hydrogel can be accomplished by mixing the precursor solution with graphene oxide solution and then going through the hydrothermal treatment, as illustrated in Figure 1. The catalysts most widely used are Fe, Co, and Ni in growing CNTs by chemical vapor deposition (CVD).²⁵ In this work, nickel was chosen and the precursor solution used was NiCl_2 solution. As shown in the Figure, chemically exfoliated graphene oxide (GO) was mixed with nickel chloride in water and the mixture was sonicated for uniform dispersion at room temperature. Heat treatment of the black-colored solution in oven for 6 hours under pressure produced a black-colored aggregate, which is a hydrogel. The hydrogel containing the nickel chloride solution was then freeze-dried for 24 hours to obtain graphene aerogel containing the nickel salt. This 3D graphene-metal salt aerogel is to be called G-MS aerogel. With this G-MS, two different methods were used to prepare two kinds of 3D CNT-bonded graphene hybrid aerogels. In one, G-MS itself, or catalyst metal salt itself, was used in growing CNTs. In the other, the catalyst metal salt was first reduced to its elemental metal by annealing (refer to experimental section for details) and this aerogel containing Ni nanoparticles is termed G-MN. The 3D CNT-bonded graphene hybrid aerogel prepared with G-MS is to be called G-CNT_A; the hybrid aerogel prepared with G-MN, G-CNT_B. In both types, one-dimensional CNTs grown on graphene would bridge the graphene layers, making the aerogels behave like a porous 3D graphene structure. Given in Figure S1 are the transmission electron microscopy (TEM) images of the interface between graphene and CNT, showing that the CVD-grown CNT is interconnected with graphene. It has been shown that CNTs grown on single layer of graphene are bonded to graphene.²⁶

Figures 2a through 2d show micrographs obtained by scan

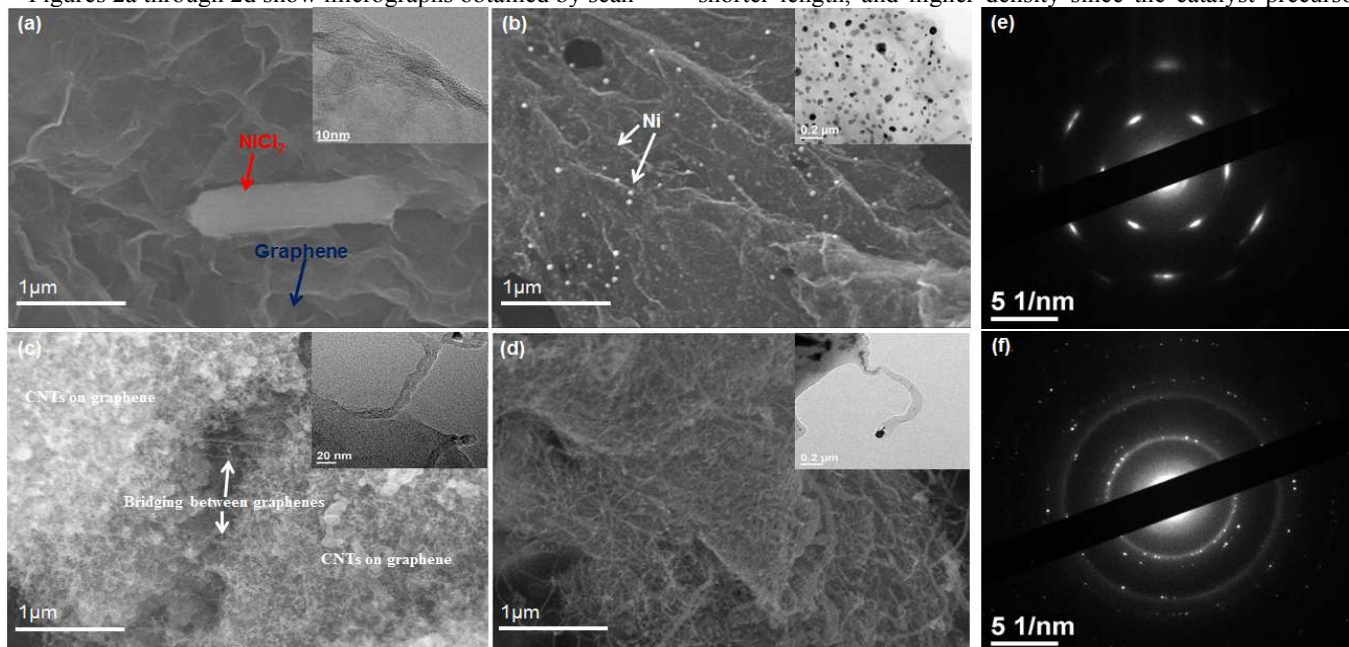


Figure 2. SEM images of 3D graphene-CNTs hybrid structure. (a) G-MS, (b) G-MN, (c) G-CNT_A and (d) G-CNT_B. The insets are TEM images. (e) and (f) electron diffraction patterns of G-MS and G-MN.

-ning electron microscopy (SEM) for G-MS, G-MN, G-CNT_A, and G-CNT_B, respectively, with the insets showing TEM images. A microparticle of nickel chloride on graphene platelets is exposed in the SEM image of Figure 2a, and the corresponding selected-area electron diffraction (SAED) pattern of the graphene platelets given in Figure 2e shows clear diffraction spots that are characteristic of crystalline order: the 6-fold pattern is consistent with a hexagonal lattice. According to the XRD pattern in Figure S3a, all of the complex diffraction peaks of the G-MS can be indexed to $\text{NiCl}_2 \cdot 6\text{H}_2\text{O}$ (JCPDS No. 025-1044). A large number of microparticles can be observed to be well-distributed on graphene platelets of the G-MS in a low magnification image of Figure S2a. A number of nickel nanoparticles present on graphene platelets are shown in Figure 2b, which is for G-MN aerogel. The aerogel of G-MS was transformed into G-MN through reduction of NiCl_2 with thermal annealing under H_2 atmosphere ($\text{NiCl}_2 + \text{H}_2 \rightarrow \text{Ni} + 2\text{HCl}$). The XRD patterns in Figure S3a give an indication of the transformation of the NiCl_2 to metallic Ni and Figure 2f shows the corresponding SAED pattern. The diffraction rings in SAED pattern of Figure 2f are made up of many diffraction spots, which indicate that Ni NPs are polycrystalline.^{27, 28} As shown in Figure 2b and the inset TEM image, Ni NPs can be observed to be distributed homogeneously on the graphene sheet and have an average diameter of 65 nm, even after strong sonication for the preparation of the TEM sample. The strong sonication had little effect on the G-MN, suggesting a relatively strong interaction between the Ni NPs and the graphene sheets.

In the process of growing CNT on G-MS to prepare G-CNT hybrid aerogel, or G-CNT_A, the metal salt is converted to its elemental nickel by hydrogen injected into the feed gas mixture of carbon source gas, growth enhancer, and carrier gas for the CVD growth of CNT. Figure 2c shows that a large number of entangled CNTs tightly cover the graphene sheets and the bonded CNTs are bridging graphenes (also refer to Fig S4 magnifying Figure 2C image). These CNTs, compared with those in G-CNT_B in Figure 2d, have a much smaller diameter, shorter length, and higher density since the catalyst precursor

particles did not go through annealing process, which causes aggregation of particles as in the case of G-CNT_B. Figure 2d shows the presence of a large number of tangled tubular structures over the surface of the graphene sheets. These CNTs are mainly multi-walled CNTs (MWNT) with a length of a few μm and outer diameter of several tens of nm. The CNT in the inset of Figure 2d has an outer diameter of 62.6 nm, which is in excellent agreement with the average size of the Ni NPs on the G-MN aerogel. The Raman spectra of GO and the 3D graphene hybrid structures are shown in Figure S3b. The spectra for GO, G-MS and G-MN exhibit two prominent peaks near 1350 and 1600 cm^{-1} corresponding to the D and G bands of graphene. The Raman spectra of the G-CNT_A and G-CNT_B clearly indicate the presence of MWCNTs with the appearance of 2D peaks at about 2780 cm^{-1} and show a decrease in the I_D/I_G ratio due to an increase in sp^2 domains resulting from the grown CNTs.

With the introduction of CNTs to bridge the gaps between graphene platelets in the hybrid aerogel, improvements in physical properties are expected. As apparent from Figure 3a and 3b, respectively, for mechanical and electrical properties, the hybrid aerogels of G-CNT_A and B are much superior to the aerogels of G-MN and G-MS that do not have bridging CNTs. Of the two structures with CNTs, G-CNT_B shows a higher elastic modulus because CNTs in G-CNT_B are larger and longer than those in G-CNT_A. The linear current (I)-voltage (V) relationship observed in Figure 3b for the 3D graphene hybrid structure indicates a high conductivity for G-CNT_A and B. Two main factors contributing to the enhancement of the electrical conductivity of G-CNT_A and B are: (1) tight contact between graphene by thermal reduction and (2) out-of-plane electron transport by CNTs bridging the gap between graphenes. Because of tighter contact, for one, G-MN aerogel shows a higher electrical conductivity than G-MS aerogel.

Shown in Figure 3c are the specific surface areas for the four aerogels. The hybrid aerogels of G-CNT_A and B have a larger specific surface area than the aerogels of G-MS and G-MN without CNTs because CNTs grown on graphene sheets have a high aspect ratio. Also, the hybrid aerogel of G-CNT_A has a CNT density higher than the hybrid of G-CNT_B and therefore it shows the largest specific surface area among the 3D

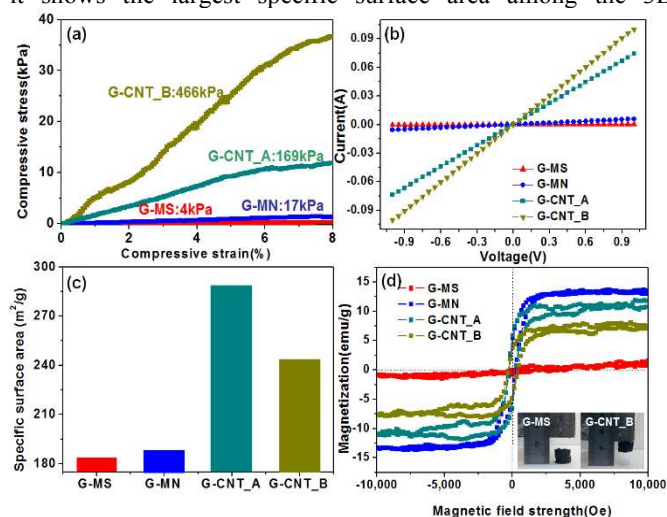


Figure 3. Properties of 3D graphene-CNTs hybrid structures. (a) Young's modulus, (b) I-V curve (c) Specific surface area (BET) (d) Room-temperature hysteresis loop of magnetization of 3D graphene-CNTs hybrid structures.

graphene hybrid structures. Mesoporous nature of the 3D graphene hybrid structures was confirmed by nitrogen sorption investigation as shown in Figure S5 and S6. For the G-MN, G-CNT_A and B, the nitrogen sorption isotherm exhibits an IUPAC (International Union of Pure and Applied Chemistry) type IV curve characteristic, indicating that there exist many meso-pores in the structures.²⁹ The pore size distributions of the structures were obtained with N₂ sorption (BJH method, mesopores measurement) and the results are shown in supplementary information (Fig S6). G-MS and G-MN structures mostly contain pores less than 2 nm in size and macropores are not present. But, G-CNT_A and B contain many mesopores. The enhancement in meso-porosity results from CNT intercalation between graphene sheets and filling of macropores with CNTs.

The magnetic property of the aerogels was of interest because there are few porous magnetic materials. To investigate the behavior, a series of magnetic hysteresis curves for 3D graphene hybrid structures were measured at room temperature, shown in Figure 3d. The aerogels of G-MN, G-CNT_A and B show ferromagnetic properties. But G-MS does not respond to magnet as shown in the inset of Figure 3d because it contains a metal salt and not the metal. The coercive force, remnant magnetization, and saturation magnetization of the structures are summarized in Table S2. Numerous Ni NPs on graphene sheets evaporated because G-CNT_A and B were exposed for a longer time than the G-MN at high temperature. Thus, saturation magnetization of the two G-CNT hybrid aerogels decreased with decreasing amount of embedded Ni NPs. To estimate the amount of Ni NPs evaporated, mass change of the aerogel was measured after annealing G-MN for a period of time that is equal to the CNT growth time (60min) but this time under only Ar atmosphere without carbon source, H₂ and water vapor. The mass has been found to decrease from 26 mg to 21 mg. This mass change resulted from evaporation of Ni NPs because the thermal reduction of graphene in inert atmosphere is insignificant.

One interesting observation we made regarding the mechanical property, which was not expected, was that the viscoelasticity is temperature-invariant from -150 °C to 450 °C, as shown in Figure S7. Viscoelasticity describes the ability of a material to both dissipate energy (viscous) and reversibly

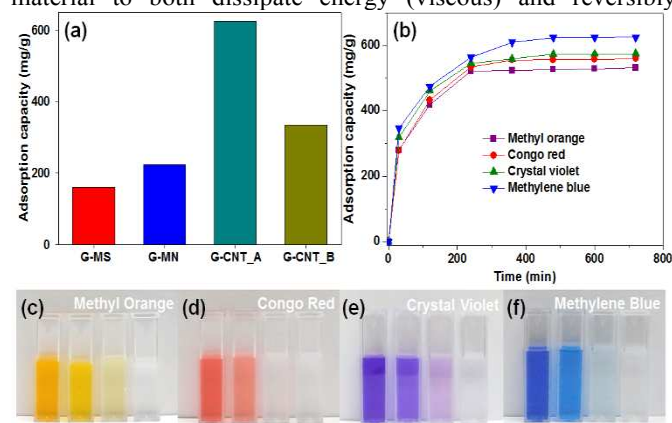


Figure 4. Adsorption of organic dye in water by 3D graphene-CNTs hybrid structures. (a) Adsorption capacity (Q) of 3D graphene-CNTs hybrid structures to the dyes. (b) Adsorption curves of four dyes (methylene blue, crystal violet, congo red and methyl orange) by G-CNT_A (c-f) color of the dye solutions according to adsorption time (from left in the each pictures, adsorption time: 0, 30, 120, 240 min).

deform (elastic).³⁰ Viscoelastic properties of rubbers, which are most widely used, are inherently temperature dependent.³¹ This is because molecular motion that is the origin of viscoelasticity is a thermally activated process. Therefore, viscoelastic materials possess a limited operational temperature range (for example, for silicone rubber it is -55 to 300 °C).³⁰ Strain dependence tests (Fig S7a and b) show that the critical strain of G-CNT_A and B, which is the strain allowing reversible deformation, was 1~7%. But, G-MS and MN show steady decline in moduli along with increase in strain, which is caused by slipping among graphenes. The reversible deformation of the G-CNT_A and B can be attributed to CNTs supporting the graphenes. The CNTs protect the structures from collapsing. Figures S7c and d show viscoelastic properties of the structures over a wide temperature range. The tests were performed at 3% strain. In the case of G-MS, the structure was seriously damaged and collapsed by chlorine gas generated from NiCl_2 contained in G-MS when the temperature was higher than 100 °C. Therefore, the viscoelastic properties of G-MS in the high temperature range could not be measured. Other aerogels show temperature-invariant viscoelasticity from -150 to 450 °C. Sudden decline in moduli over 450 °C is due to structure collapse caused by rapid oxidation of graphenes and CNTs. Note that the structures are tested in air in the high temperature range. We demonstrate here that the assembly of CNTs and graphenes with their exceptional mechanical and thermal stability can lead to thermally stable viscoelasticity.

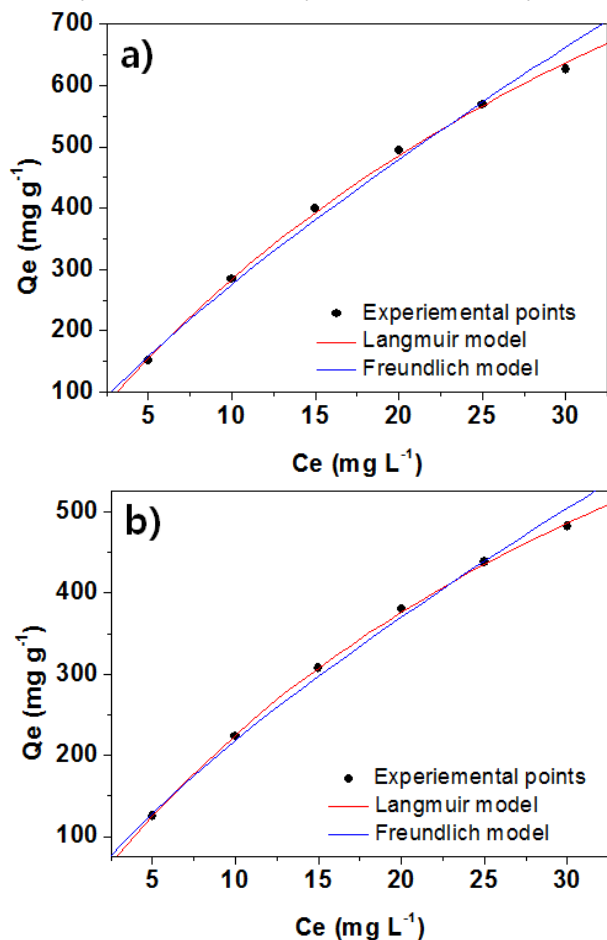


Figure 5. Adsorption isotherms of a) MB and b) MO on G-CNT_A simulated by the Langmuir model (red line) and Freundlich model (blue line).

The high specific surface area that these aerogels possess bodes well for high adsorption capacity. As shown in Figure 4a, the hybrid aerogel of G-CNT_A having the largest surface area among the 3D structures shows the highest adsorption capacity of methylene blue (MB) (626 mg/g). The adsorption is due to π - π interaction and van der Waals force between nano-carbon materials (i.e. graphene and CNT) and organic dyes.^{24, 32} Therefore, the larger the surface area of structure is, the more dye molecules the structure adsorbs. Movie 1 shows that rotating G-CNT_A by an external magnetic stirrer helps removing the dye from water. The rotation of the structure by an external magnet enables fast adsorption of dye molecules because of circulation of the dye solution inside and outside the structure. After the adsorption, the structure is easily collected by the magnet. Thus, the magnetism of the structure is very useful for adsorption and collection in water treatment.

It is known that reduced graphene oxide (rGO) removes anionic dyes.³² It is also known that multi-walled carbon nanotube composite containing magnetic iron oxide nanoparticles is a good adsorbent of cationic dyes.³³ The hybrid aerogels of CNT-bonded graphene, therefore, could be excellent adsorbents of both anionic and cationic dyes. To prove the point, adsorption capacities for two anionic dyes (methyl orange [MO] and congo red [CR]) and two cationic dyes (crystal violet [CV] and methylene blue [MB]) in aqueous solution were determined as shown in Figure 4b. The hybrid aerogel of G-CNT_A was used for the purpose in light of the high capacity discussed above for methylene blue (626 mg/g).

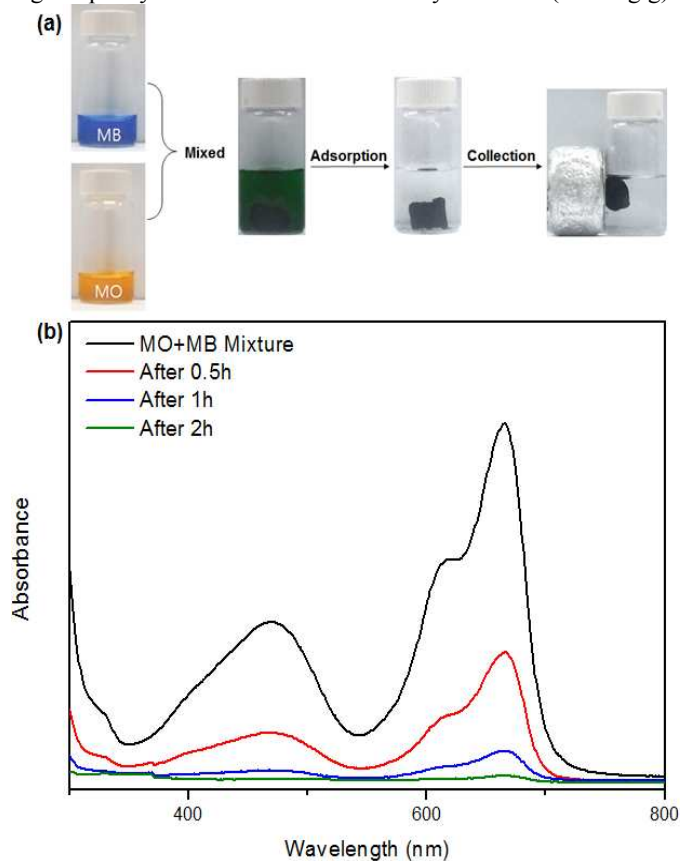


Figure 6. Simultaneous adsorption of positive and negative charged dyes. a) Photographs of simultaneous adsorption of MB/MO dyes from the mixture solution by G-CNT_A and b) a trend of its corresponding UV-Vis spectra according to adsorption time.

This capacity compares with that of CNT-graphene aerogel (190mg/g) in which CNTs are physically mixed with no bonding between CNT and rGO.²⁴ This mixture aerogel based on electrostatic adsorption is an adsorbent much better for positive dyes, the adsorption capacity for negative dyes being at least an order of magnitude smaller because of residual functional groups.²⁴ Poly-dopamine coated graphene showed the highest adsorption capacity of all adsorbents reported so far for MB (1800mg/g).³⁴ However, it adsorbs dyes only with Eschenmoser structure. Furthermore, it is impossible to recycle because adsorption process is based on chemical reaction between poly-dopamine and dye molecules. As shown in Figure 4b, the adsorption capacity of G-CNT_A for the other positive dye of crystal violet is 575 mg/g, which compares with that achieved with the reduced graphene on which CNTs are chemically bonded (228mg/g).³⁵ The capacities for negative dyes are 560 (congo red) and 532 (methyl orange) mg/g, which are much larger than those of other graphene-based adsorbents (congo red:33.66³⁶, methyl orange: 101.34³⁷ mg/g). The progression of dye adsorption with time is shown in Figure 4c through 4f for the four dyes tested. The color change shows that the water solution is cleared of dye in about 240 min in all cases (also refer to UV-vis absorption spectra of the solutions in Figure S8). It is noted in this regard that G-CNT_A contains only 1% oxygen as shown in the EDS data in Figure S9 and Table S1, indicating that there are not many oxygen-related functional groups remaining as a result of the hydrothermal and thermal treatments.

To look into the nature of adsorption, adsorption isotherms were obtained at room temperature. Two different adsorption isotherms, Langmuir³⁸ and Freundlich³⁹ model, were used to fit the experimental adsorption data for MB and MO on G-CNT_A. The adsorption isotherm indicates how adsorption molecules are distributed between the liquid phase and the solid phase when the adsorption process reaches an equilibrium state. As shown in Figure 5, the data for the two dyes were well fitted with Langmuir model rather than Freundlich model under different concentrations studied. The results indicate that during the adsorption process, monolayer of the dyes covers a homogeneous surface and there is no subsequent interaction between adsorbed and non-adsorbed dye molecules.⁴⁰

Adsorption ability of the hybrid aerogel irrespective of dye charge enables simultaneous adsorption of positively and negatively charged dyes. To demonstrate such capability, a mixed solution containing MB/MO in 1:1 volume ratio was prepared. Then G-CNT_A was put into the solution. Figure 6a shows that both dyes oppositely charged are removed by the hybrid aerogel. The solution concentration was measured by UV-Vis absorption as a function of adsorption time, shown in Figure 6b. The UV-vis spectra clearly show that absorption peaks of MB (636nm) and MO (464nm) completely disappears after 2h, indicating that both MB and MO have been removed by G-CNT_A. The used adsorbent was simply collected by magnet.

To demonstrate regeneration and reuse of the spent adsorbent, the adsorbed MB dye molecules on G-CNT_A were desorbed in cetyltrimethylammonium bromide (CTAB, surfactant) solution and then the structure was reused for the adsorption of MB dye. The structure was rinsed multiple times in CTAB solution before reuse. The color of the original CTAB solution is transparent. Figure S10a shows the color of CTAB solution changes to blue due to the dye desorbed from the G-CNT_A after the first rinse but after 8th rinse, the solution is clear, indicating that the aerogel is free of the dye. Shown in

Figure S10b are the UV-vis spectra of the solution containing dye, the solution made clear of dye by fresh hybrid aerogel, and the solution made clear of dye by regenerated hybrid aerogel. The UV-vis spectra show that the peak of the original MB solution at 670 nm completely disappeared after the adsorption. Even when the G-CNT_A is reused, the peak is not observed in the spectra (2nd_abs. curve in Figure S10b), indicating recyclability of the G-CNT_A aerogel. The inset in Figure S10b shows the pictures of the solution, in successive order, the original solution, the solution after dye removal with fresh aerogel, the solution resulting with the use of recycled hybrid aerogel.

The 3D graphene hybrid structures are superhydrophobic and meso-porous, which makes them excellent candidates for oil absorption. Hashim et al. reported covalently bonded CNT sponge with meso-porosity has a high oil absorption capacity.¹⁶ Figure S11 shows oil/solvent uptake performance of the 3D graphene hybrid structures. The snapshots of movie 2 given in Figure S11a show a sequence of selective absorption of toluene by G-CNT_A on water surface. After selectively absorbing toluene in one spot, the structure is moved to another spot by an external magnet and allowed to absorb toluene. The magnetic nature of the structure can be useful for collecting and moving the structures on water surface. Recyclability is demonstrated in Figure S12 for toluene absorption. These results show that G-CNT structures are a promising adsorbent material for oil-water separation.

Conclusions

We have introduced CNT-bonded graphene aerogels for the purpose of making graphene aerogels more versatile and attractive in diverse applications by improving their physical properties. Unlike a physical mixture of CNTs and graphene, the CNTs in the aerogels are bonded to graphene. As a result, the elastic modulus of the aerogel is increased by more than an order of magnitude when compared with the aerogel without CNTs. The electrical conductivity is also increased by more than two orders of magnitude. The specific surface area is increased by 32% and 57% for the two types of the hybrid aerogels prepared by different procedures and both aerogels are endowed with mesoporous structure. The catalyst used for the CNT growth on graphene makes the aerogel magnetic, which can be used for separation and transport of the aerogel. A surprise was that the hybrid aerogels have viscoelasticity that is invariant with temperature between -150 °C and 450 °C.

The hybrid aerogel with large surface area and high mechanical strength is suitable for water purification. Therefore, the hybrid aerogel with a larger specific surface area was utilized to demonstrate its utility as a reusable water treatment material. As a reusable adsorbent, its adsorption capacity is by far the highest ever reported for graphene-based adsorbents. It is also the first adsorbent known for adsorbing both cationic and anionic dyes simultaneously. It was also found that it can efficiently and selectively separate oils and organic solvents from water. The other hybrid aerogel with a lower specific surface area but with much better mechanical and electrical properties (G-CNT_B) would prove to be valuable in the fields of biotechnology and electrochemistry, such as drug-delivery, tissue scaffolds, bionic nanocomposites, and supercapacitors and batteries.

Notes and references

^a School of Mechanical and Aerospace Engineering, Seoul National University, Daehak-dong, Gwanak-gu, Seoul, 151-742, Republic of Korea. *E-mail: yongkim@snu.ac.kr*

^b Department of chemistry education, Seoul National University, Daehak-dong, Gwanak-gu, Seoul, 137-42, Republic of Korea

^c School of Chemical and Biological Engineering, Seoul National University, Institute of Chemical Processes (ICP), Daehak-dong, Gwanak-gu, Seoul, 151-742, Republic of Korea.

Electronic Supplementary Information (ESI) available: TEM images of interface between graphene and CVD-grown CNT, SEM images of 3D graphene hybrid structures at low-magnification. XRD, Raman and EDS spectra (elemental composition table by EDS), SEM images on CNTs bridging between graphenes. Nitrogen sorption isotherms and pore size distribution of 3D graphene hybrid structures. Viscoelastic properties (storage and loss modulus according to temperature). UV-vis spectra of the dye solutions according to absorption time, solvent/oil absorption capacity and regeneration for dye adsorption and solvent/oil absorption and a summary of properties of 3D graphene hybrid structures. See DOI: 10.1039/b000000x/

ACKNOWLEDGMENT

This research was supported by the National Research Foundation of Korea (Grants 2014R1A2A1A05007760), Defense Acquisition Program Administration and Agency for Defense Development under Contract UD100048JD, and the Brain Korea 21 Plus Project in 2014. The authors also acknowledge support from the Institute of Advanced Aerospace Technology at Seoul National University. The first author thank Prof. Chung-Hak Lee and Mr. Jaewoo Lee at School of Chemical and Biological Engineering, Seoul National University for UV-Vis measurement, and Prof. Hong H. Lee at School of Chemical and Biological Engineering, Seoul National University for revision of the manuscript.

1. Y. Xu, K. Sheng, C. Li and G. Shi, *ACS nano*, 2010, **4**, 4324-4330.
2. C.-C. Ji, M.-W. Xu, S.-J. Bao, C.-J. Cai, Z.-J. Lu, H. Chai, F. Yang and H. Wei, *J. Colloid Interface Sci.*, 2013, **407**, 416-424.
3. W. Chen, S. Li, C. Chen and L. Yan, *Adv. Mater.*, 2011, **23**, 5679-5683.
4. L. Ren, K. Hui and K. Hui, *Journal of Materials Chemistry A*, 2013, **1**, 5689-5694.
5. L. Chen, X. Wang, X. Zhang and H. Zhang, *J. Mater. Chem.*, 2012, **22**, 22090-22096.
6. J. Li, J. Li, H. Meng, S. Xie, B. Zhang, L. Li, H. Ma, J. Zhang and M. Yu, *Journal of Materials Chemistry A*, 2014.
7. J. Arellano, *JNanoR*, 2009, **5**, 201-211.
8. E. F. Sheka and L. A. Chernozatonskii, *J. Comput. Theor. Nanosci.*, 2010, **7**, 1814-1824.
9. Y. Mao and J. Zhong, *New J. Phys.*, 2009, **11**, 093002.
10. V. Varshney, S. S. Patnaik, A. K. Roy, G. Froudakis and B. L. Farmer, *ACS nano*, 2010, **4**, 1153-1161.
11. G. K. Dimitrakakis, E. Tyljanakis and G. E. Froudakis, *Nano Lett.*, 2008, **8**, 3166-3170.
12. L. L. Zhang, Z. Xiong and X. Zhao, *Acs Nano*, 2010, **4**, 7030-7036.
13. F. Du, D. Yu, L. Dai, S. Ganguli, V. Varshney and A. Roy, *Chem. Mater.*, 2011, **23**, 4810-4816.
14. Z. Fan, J. Yan, L. Zhi, Q. Zhang, T. Wei, J. Feng, M. Zhang, W. Qian and F. Wei, *Adv. Mater.*, 2010, **22**, 3723-3728.
15. H. Hu, Z. Zhao, W. Wan, Y. Gogotsi and J. Qiu, *Adv. Mater.*, 2013, **25**, 2219-2223.
16. D. P. Hashim, N. T. Narayanan, J. M. Romo-Herrera, D. A. Cullen, M. G. Hahm, P. Lezzi, J. R. Suttle, D. Kelkhoff, E. Munoz-Sandoval and S. Ganguli, *Scientific reports*, 2012, **2**.
17. W. Feng, M. Qin, P. Lv, J. Li and Y. Feng, *Carbon*, 2014, **77**, 1054-1064.
18. J. Wen, Y. Li and W. Yang, *Vacuu*, 2014, **101**, 271-274.
19. M.-Q. Zhao, X.-F. Liu, Q. Zhang, G.-L. Tian, J.-Q. Huang, W. Zhu and F. Wei, *ACS nano*, 2012, **6**, 10759-10769.
20. X. Dong, B. Li, A. Wei, X. Cao, M. B. Chan-Park, H. Zhang, L.-J. Li, W. Huang and P. Chen, *Carbon*, 2011, **49**, 2944-2949.
21. S. Li, Y. Luo, W. Lv, W. Yu, S. Wu, P. Hou, Q. Yang, Q. Meng, C. Liu and H. M. Cheng, *Advanced Energy Materials*, 2011, **1**, 486-490.
22. S. Chen, P. Chen and Y. Wang, *Nanoscale*, 2011, **3**, 4323-4329.
23. W. S. Hummers Jr and R. E. Offeman, *J. Am. Chem. Soc.*, 1958, **80**, 1339-1339.
24. Z. Sui, Q. Meng, X. Zhang, R. Ma and B. Cao, *J. Mater. Chem.*, 2012, **22**, 8767-8771.
25. C. J. Lee, J. Park and J. A. Yu, *Chem. Phys. Lett.*, 2002, **360**, 250-255.
26. Y. Zhu, L. Li, C. Zhang, G. Casillas, Z. Sun, Z. Yan, G. Ruan, Z. Peng, A.-R. O. Raji and C. Kittrell, *Nature communications*, 2012, **3**, 1225.
27. A. Fernández and T. C. Rojas, *Mater. Trans.*, 2003, **44**, 2055-2061.
28. W. Zhiqiang, X. Tiandong, M. Jun, F. Wangjun, D. Jianfeng, W. Qing and Y. Pengxun, *Mater. Charact.*, 2007, **58**.
29. K. S. Sing, *Pure Appl. Chem.*, 1985, **57**, 603-619.
30. M. Xu, D. N. Futaba, T. Yamada, M. Yumura and K. Hata, *Science*, 2010, **330**, 1364-1368.
31. R. S. Lakes, *Viscoelastic materials*, Cambridge University Press, 2009.
32. G. Ramesha, A. Vijaya Kumara, H. Muralidhara and S. Sampath, *J. Colloid Interface Sci.*, 2011, **361**, 270-277.
33. J.-L. Gong, B. Wang, G.-M. Zeng, C.-P. Yang, C.-G. Niu, Q.-Y. Niu, W.-J. Zhou and Y. Liang, *J. Hazard. Mater.*, 2009, **164**, 1517-1522.
34. Z. Dong, D. Wang, X. Liu, X. Pei, L. Chen and J. Jin, *Journal of Materials Chemistry A*, 2014, **2**, 5034-5040.
35. M. Kotal and A. K. Bhowmick, *The Journal of Physical Chemistry C*, 2013, **117**, 25865-25875.
36. Y. Yao, S. Miao, S. Liu, L. P. Ma, H. Sun and S. Wang, *Chem. Eng. J.*, 2012, **184**, 326-332.
37. N. Li, M. Zheng, X. Chang, G. Ji, H. Lu, L. Xue, L. Pan and J. Cao, *J. Solid State Chem.*, 2011, **184**, 953-958.
38. I. Langmuir, *J. Am. Chem. Soc.*, 1918, **40**, 1361-1403.
39. H. M. F. Freundlich, *Z. Phys. Chem.*, 1906, **57**, 385-470.
40. A. Rodríguez, J. García, G. Ovejero and M. Mestanza, *J. Hazard. Mater.*, 2009, **172**, 1311-1320.